Abhishek Pandala[1], S. Shivaprasad[1]*, C.V. Krishnamurthy[1,2], Krishnan Balasubramaniam[1]

[1]Centre for Non-Destructive Evaluation, Department of Mechanical Engineering, Indian Institute of Technology, Madras, Chennai, India
[2]Department of Physics, Indian Institute of Technology, Madras, Chennai, India

Robust and efficient finite-difference-time-domain modelling of the propagation of nonlinear elastic waves

Niezawodne i wydajne modelowanie propagacji nieliniowych fal sprężystych metodą różnic skończonych w dziedzinie czasu

ABSTRACT

A robust finite-difference-time-domain (FDTD) scheme to model the non-linear elastic wave propagation in a homogeneous isotropic material is presented. A formulation based on rotated staggered grid scheme in a displacement-velocity-stress configuration incorporating both geometric and material nonlinearities is proposed. By adopting a Parsimonious algorithm, the computational memory requirement is reduced by 50%. Simulations are accelerated by exploiting massive data parallelism innate to the FDTD approach using parallel computation on Graphical Processing Units with NVIDIA CUDA's API. For the proposed numerical scheme, the grid convergence criterion and accuracy over propagating distances are investigated. The study is also extended to determine the contribution from geometric and material models at various input amplitude levels. The time and frequency domain signals obtained from the proposed scheme are verified with a commercial finite element solver. The simulation runtimes for an Aluminium sample of dimensions 20 mm x 10 mm using a 5 MHz pulse is of the order of one minute, which makes the proposed numerical scheme attractive to model nonlinear elastic waves in large domains.

STRESZCZENIE

W artykule przedstawiono odporny schemat metody różnic skończonych w dziedzinie czasu (FDTD) do modelowania propagacji nieliniowych fal sprężystych w jednorodnym materiale izotropowym. Zaproponowano podejście oparte na rotowanych siatkach przestawnych w układzie przemieszczenie-prędkość-naprężenie obejmującym zarówno nieliniowość geometryczną, jak i materiałową. Zastosowanie algorytmu redukcji oszczędnej, zmniejszyło zapotrzebowanie na pamięć obliczeniową o 50%. Symulacje są przyspieszane przez wykorzystanie olbrzymiego paralelizmu danych wbudowanego w podejście FDTD z wykorzystaniem obliczeń równoległych na jednostkach przetwarzania graficznego (GPU) wyposażonych w interfejs API NVIDIA CUDA. Dla proponowanego schematu numerycznego badane jest kryterium zbieżności siatki i dokładność w funkcji odległości propagacji. Badanie rozszerzono również w celu określenia wkładu modeli geometrycznych i materiałowych na różnych poziomach amplitudy wejściowej. Sygnały w dziedzinie czasu i częstotliwości uzyskane z proponowanego schematu są weryfikowane za pomocą komercyjnego oprogramowania wykorzystującego metodę elementów skończonych. Czasy pracy dla symulacji propagacji impulsu o częstotliwości 5 MHz w próbce aluminium o wymiarach 20 mm x 10 mm są rzędu jednej minuty, co sprawia, że proponowany schemat liczbowy jest atrakcyjny dla modelowania nieliniowych fal sprężystych w dużych domenach.

1. Introduction

Interatomic forces that bind solids determine the responses to external forces. The interatomic potentials can be very well approximated as quadratic in displacements, for sufficiently small displacements of atoms from their equilibrium positions. As a result, the response to small external forces can be reasonably approximated to be linear in displacements. For microscopically homogeneous solids subject to small external forces, a description in terms of linear response would be a reasonable first approximation. However, there are a wide range of solids, natural and synthetic, that are not homogenous in a strict microscopic sense. Microscopically inhomogeneous features such as dislocations, grain boundaries, voids, micro-cracks, pores exist. Solids having these internal features are in reasonably stable equilibrium and may be described as macroscopically homogenous media in some average sense.

There exists considerable experimental evidence to indicate that such macroscopically homogeneous media respond nonlinearly to applied forces. Several of the examples of nonlinear effects reported in the literature include higher harmonics generation[1,2], resonance shift in frequency[3], amplitude-dependent and non-classical dissipation[4], DC response and subharmonic generation[5], wave modulation and frequency mixing[6]. Nonlinear acoustic and elastic waves have been investigated extensively for past few decades on grained materials[7], and rocks[8], in areas relating to geology[9], seismology[10], biophysics[11], biomedical engineering[12], lithotripsy and acoustic physiotherapy of soft tissues[13] and nondestructive testing of polycrystalline and composite media[14].

Historically, the nonlinear theories have been classified

*Correspondence author. E-mail: prsd.shiva@gmail.com

into two: classical theory, which accounts for the higher order elastic terms in the Hooke's law and the non-classical theory which includes mechanisms like stress-strain hysteresis and contact acoustic nonlinearities(CAN)[5].

Two types of classical nonlinearity have been reported in the literature[4,15,16], i.e. geometric (kinematic) and material (physical) nonlinearities. The former accounts for the gradient of the strain-displacement relation, whereas the latter is the result of the nonlinear stress-strain function (i.e. the third- and higher-order terms in elastic energy). The contribution of geometrical nonlinearity in solids has been known to be much smaller than the material nonlinearity, and, hence, has usually been neglected[17].

Among the various applications of nonlinear acoustic and elastic waves described earlier, the most exciting potential is believed to be in characterising materials nondestructively. In last few decades, researchers have been able to experimentally relate the acoustic nonlinearity parameter, β with microscopically inhomogeneous features such as dislocations, grain boundaries, precipitates, voids, micro-cracks formed due to various damages mechanism like fatigue, creep, thermal aging and radiation damage which can be related to the third-order elastic(TOE) constants[18,19].

The majority of literature deals with the experimental determination of the nonlinearity parameter using harmonic generation technique. The non-linearity parameter obtained from experiments is the combined effect of many microscopic factors as well as instrumentation non-linearity. The individual contribution of each of the microscopic factors to the non-linearity parameter is not entirely understood. Numerical simulations can provide a better insight into nonlinear wave characteristics by allowing for the study of individual contributions to non-linearity. A variety of numerical methods have been employed for examining the nonlinear wave propagation through homogeneous isotropic media, including the finite element (FE) method [20–23], the elastodynamic finite integration technique[24] and the finite difference(FD) method[25,26]. Researchers in the past have mostly resorted to various commercially available explicit/implicit FE solvers for dealing with such problems. For instance, Chillara and Lissenden [20] solved a two-dimensional FE model using the implicit solver, while Rauter and Lammering[22] and Xiang et al. [23] adopted an explicit solver, all of them incorporating TOE constants to account for the nonlinear effects. Drewry and Wilcox[21] on the other hand, looked at computationally less intensive one-dimensional FE models, underlining various signal processing protocols for obtaining the quantitative value of nonlinearity parameter. Commercial software packages based on FEM are memory intensive. Implicit solvers are also CPU time intensive as the computational domain increases.

Little work has been done in the past to develop finite difference time domain(FDTD) numerical models for elastic wave propagation through nonlinear media. Matsuda and Biwa [25,26] proposed a two-dimensional finite difference time domain(FDTD) model using a Standard Staggered Grid(SSG)[27,28] by incorporating both geometric and material nonlinearities. For anisotropic as well as nonlinear media, SSG requires interpolation of stress and strain [25]. The rotated staggered grid(RSG) FDTD scheme[29] overcomes this shortcoming by placing the density and material parameters at the same location corresponding to velocity and stress components respectively. There have been efforts in the past to exploit the graphics processing cards to accelerate simulations for linear elastodynamic problems [30–33].

The scope of the present work is to develop a robust and time-efficient two-dimensional RSG-FDTD scheme capable of modelling the non-linear response of the material while exploiting massive data parallelism innate to the FDTD approach. A formulation to deal with finite amplitude wave propagation based on FDTD method considering both the geometric and material nonlinearities is presented here. The geometric nonlinear model adopts a Signorini's model[34], while the complete nonlinear model considers Lagrangian stress and strain tensors, accounting for both geometric and material nonlinearity. The gridding convergence requirements to capture the higher harmonics components are presented. Signal stability as a function of propagation distance, evolution of higher harmonics with input amplitude as well as with propagation distance are described. The time and frequency domain signals obtained from the proposed scheme are verified with the commercial FE solver. The article has been organised as follows. Section 2 presents the theoretical formulation of nonlinear wave propagation. Section 3 explains the FDTD scheme implemented in this study. Section 4 describes the numerical model, grid convergence and propagation aspects. The results are discussed in Section 5 and conclusions are presented in Section 6.

Tab. 1. Different models presented in this study
Tab. 1. Różne modele przedstawiane w niniejszej pracy

Model	Strain Measure	Elastic Constants
Linear Elastic (LIN)	Cauchy Strain	Second Order
Geometric Nonlinear (GNL)	Almansi Hamel Strain	Second Order
Material Nonlinear (MNL)	Lagrangian Strain	Second and third Order

2. Non-Linear Elastodynamics - Theoretical Formulations

We consider three different models for the present study. First, a linear elastic model (LIN) is used considering Cauchy strain as the strain measure coupled with second-order elastic constants. Second, geometric nonlinear model (GNL) is introduced by adopting Signorini's model[34] relating finite strain tensor and Cauchy's stress tensor which is coupled with second-order elastic constants. Third, a complete nonlinear model comprising both geometric and material nonlinearity called Material Nonlinear model(MNL) is used. Here, the Lagrangian strain is used as the strain measure and is combined with second and third order elastic constants. The models considered in this study are shown in Table 1.

2.1 Linear Elastic Model

In this model, a linear relationship between stress and strain is assumed and Cauchy strain is used as the strain

measure [35]. The linearized strain tensor is,

$$\varepsilon_{ij} = \frac{1}{2}\left(u_{i,j} + u_{j,i}\right) \tag{1}$$

where ε_{ij} is the strain, u_i is the displacement and $u_{i,j} = \dfrac{\partial u_i}{\partial u_j}$.

Following the constitutive relationship for elastic isotropic solids we have,

$$\sigma = 2\mu\varepsilon + \lambda\, tr(\varepsilon)I \tag{2}$$

The simplified constitutive equations turn out to be

$$\tau_{xx} = \left(\lambda + 2\mu\right)u_{x,x} + \left(\lambda\right)u_{z,z} \tag{3}$$

$$\tau_{zz} = \left(\lambda + 2\mu\right)u_{z,z} + \left(\lambda\right)u_{x,x} \tag{4}$$

$$\tau_{xz} = \tau_{zx} = \mu\left(u_{x,z} + u_{z,x}\right) \tag{5}$$

where λ and μ are the Lame elastic constants and τ_{ij} is the stress.

2.2 Geometric Nonlinear Model

Here, instead of the linearized strain, a finite strain tensor is used here. Signorini's model[34] relating the finite strain tensor (Almasi-Hamel strain) and Cauchy's stress tensor is employed in this formulation. The third order elastic constants are not considered. The finite strain tensor in terms of displacement gradient is,

$$\varepsilon_{ij} = \frac{1}{2}\left(u_{i,j} + u_{j,i} - u_{k,i}u_{k,j}\right) \tag{6}$$

The constitutive equations concerning two-dimensional non-linear wave propagation following[36] are,

$$\tau_{xx} = \frac{\lambda + 2\mu}{2}\left[2u_{x,x} - u_{x,x}^2 - u_{z,x}^2\right] + \frac{\lambda}{2}\left[2u_{z,z} - u_{x,z}^2 - u_{z,z}^2\right] \tag{7}$$

$$\tau_{zz} = \frac{\lambda + 2\mu}{2}\left[2u_{z,z} - u_{x,z}^2 - u_{z,z}^2\right] + \frac{\lambda}{2}\left[2u_{x,x} - u_{x,x}^2 - u_{z,x}^2\right] \tag{8}$$

$$\tau_{xz} = \tau_{zx} = \mu\left[u_{x,z} + u_{z,x} - u_{x,x}u_{x,z} - u_{z,x}u_{z,z}\right] \tag{9}$$

2.3 Material Nonlinear Model

For the Material Nonlinear model, the governing equations of motion, the displacement – velocity relation, and the stress- strain relation can be written by[15]

$$\rho\frac{\partial v_i}{\partial t} = \frac{\partial P_{ij}}{\partial X_j} \tag{10}$$

$$\frac{\partial u_i}{\partial t} = v_i \tag{11}$$

$$P_{ij} = C_{ijkl}\frac{\partial u_k}{\partial X_l} + \frac{1}{2}\left(C_{ijklmn} + C_{ijln}\delta_{km} + C_{jnkl}\delta_{im} + C_{jlmn}\delta_{ik}\right)\frac{\partial u_k}{\partial X_l}\frac{\partial u_m}{\partial X_n} \tag{12}$$

where X_i is the Lagragian coordinates, v_i the velocities and P_{ij} are the components of the nonsymmetric first Piola-Kirchoff stress tensor. For an isotropic material, the second- and third-order stiffness tensors are given as,

$$C_{ijkl} = \lambda\delta_{ij}\delta_{kl} + 2\mu I_{ijkl} \tag{13}$$

$$C_{ijklmn} = \frac{A}{2}\left(\delta_{ik}I_{jlmn} + \delta_{il}I_{jkmn} + \delta_{jk}I_{ilmn} + \delta_{jl}I_{ikmn}\right) + 2B\left(\delta_{ij}I_{klmn} + \delta_{kl}I_{mnij} + \delta_{mn}I_{ijkl}\right) + 2C\delta_{ij}\delta_{kl}\delta_{mn} \tag{14}$$

where A, B and C are the third-order elastic constants for an isotropic material following Landau and Lifshitz[37], δ_{ij} is the Kronecker's delta function and $I_{ijkl} = \frac{1}{2}\left(\delta_{ik}\delta_{jl} + \delta_{il}\delta_{jk}\right)$.

In simplified terms, equation (12) can be expressed as

$$\tau_{xx} = \left(\lambda + 2\mu\right)u_{x,x} + \left(\lambda\right)u_{z,z} + d_1\left(u_{x,x}\right)^2 + d_2\left(2u_{x,x} + u_{z,z}\right)u_{z,z} + d_3\left(u_{z,x}^2 + u_{x,z}^2\right) + d_4\left(u_{x,z}u_{z,x}\right) \tag{15}$$

$$\tau_{zz} = \left(\lambda + 2\mu\right)u_{z,z} + \left(\lambda\right)u_{x,x} + d_1\left(u_{z,z}\right)^2 + d_2\left(2u_{z,z} + u_{x,x}\right)u_{x,x} + d_3\left(u_{x,z}^2 + u_{z,x}^2\right) + d_4\left(u_{x,z}u_{z,x}\right) \tag{16}$$

$$\tau_{xz} = \mu\left(u_{x,z} + u_{z,x}\right) + \left(u_{x,x} + u_{z,z}\right)\left(2d_3u_{x,z} + d_4u_{z,x}\right) \tag{17}$$

$$\tau_{zx} = \mu\left(u_{x,z} + u_{z,x}\right) + \left(u_{x,x} + u_{z,z}\right)\left(2d_3u_{z,x} + d_4u_{x,z}\right) \tag{18}$$

where,

$$d_1 = \frac{3}{2}\lambda + 3\mu + A + 3B + C\ ; d_2 = \frac{1}{2}\lambda + B + C$$

$$d_3 = \frac{1}{2}\lambda + \mu + \frac{1}{4}A + \frac{1}{2}B\ ; d_4 = \mu + \frac{1}{2}A + B \tag{19}$$

It is to be noted that the stress tensor in the case of material nonlinearity is not symmetric. The elastodynamic equations for two-dimensional problem, in the absence of body forces, are given by,

$$\rho\dot{v}_x = \tau_{xx,x} + \tau_{xz,z} \tag{20}$$

$$\rho\dot{v}_z = \tau_{zx,x} + \tau_{zz,z} \tag{21}$$

$$v_x = \dot{u}_x \tag{22}$$

$$v_z = \dot{u}_z \tag{23}$$

3. Finite Difference Time Domain (FDTD) Formulation

3.1 Rotated Staggered Scheme (RSG)

In this section, the 2D Heterogeneous Explicit Parsimonious Rotated Staggered Grid Scheme is described. The RSG finite difference scheme was proposed by Saenger et al. [29], and it has been successfully applied in seismic modelling of elastic, viscoelastic, isotropic and anisotropic media[38]. In the RSG unit cell, all the velocity (and displacement) components are at the same location and the stress components at the other location (see Figure 1). Correspondingly, density is located at the same position as velocity and material parameters are located at the same position as stress. This gridding scheme is advantageous in modelling non-linear response of materials as well as anisotropic crystal systems with symmetry less than Orthotropic. It is to be noted that non-linearity and anisotropy of a material can also be modelled using the Standard Staggered Grid(SSG) [27,28], but requires interpolation of components[25,39]. The present scheme is also numerically stable with the existence of high contrast heterogeneities like voids, cracks, inclusions and the presence of more than one medium (fluid-solid contact). The application of boundary condition whether welded interface or free-surface boundary condition, is straightforward in the heterogeneous formulation of the RSG Scheme. The major disadvantage of using RSG scheme is a stricter grid dispersion criterion, i.e., a higher sampling ratio is needed to achieve the same level of accuracy as obtained by a conventional SSG [40]. This leads to increased computational memory requirements and consequently large simulation times. Both these issues are addressed in this article by adopting a Parsimonious scheme and accelerating the simulations on Graphical Processing Units respectively.

Compared to the SSG scheme, the RSG method rotates the finite differential operators to the elementary cell in the diagonal directions first, and then, the standard FD operator is calculated by the linear combination of these operators. A detailed description of the RSG scheme can be found in

ref.[29]. We adopt a second order update in space and first-order update in time. The extension to higher order spatial derivatives is straightforward.
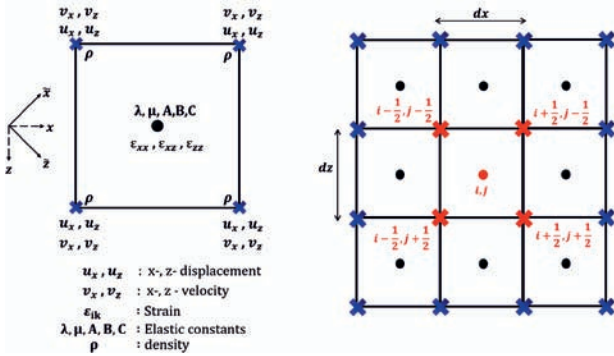

Fig. 1. Rotated Staggered gridding scheme
Rys. 1. Schemat obróconej siatki przestawnej

3.2 Parsimonious Scheme

There are various numerical formulations of the above governing equations: Velocity-stress, Displacement-Velocity-Stress, Displacement-Stress and Displacement-Displacement [41]. We develop an algorithm by adapting a Displacement-Velocity-Stress (DVS) scheme. The proposed scheme is staggered in time where displacements are stored at integral timesteps and velocities are stored at half-integral timesteps leading to a recursive time-marching algorithm (as shown in Figure 2). Equations (3-5), (7-9) and (15-18) are used to compute the stress values from displacement at integral timesteps. Equations (20-21) are used to update the velocities at half timesteps from the stress values, and finally, Equations (22-23) are used to evaluate displacement at the next integral timestep. In order to reduce the computational memory requirement, we employ the parsimonious staggered grid [42][43]. It is not a gridding scheme in itself, but rather an algorithm to reduce computational memory requirement. Since in the DVS formulation, no temporal derivatives involving stress exist, there is no need to store stress tensor components for successive timesteps. This is the prime reason for parsimony. The scheme necessitates storing only displacement components and velocity components reducing the computational memory to 50%.
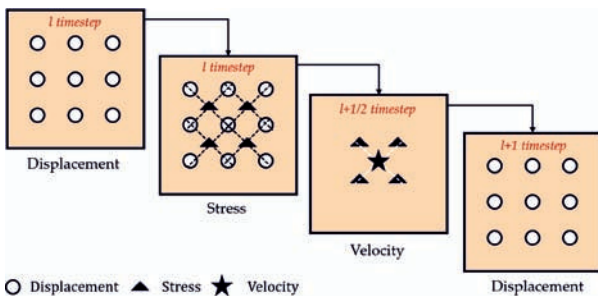

Fig. 2. Parsimonious gridding scheme
Rys. 2. Schemat redukcji oszczędnej

Stress components are evaluated but not stored for subsequent timesteps. The parsimonious scheme has memory requirements similar to that of a collocated grid [44] but exploits the numerical stability and accuracy of a complete[27] and partial staggered grid[29]. The bottleneck is that programming is much more involved and redundant computations are performed between adjacent grid points increasing the computational time. This increase in computational time is compensated by performing parallel computations on Graphical Processing Units exploiting the massive data parallelism innate to the FDTD approach. A complete set of discretized FD equations for geometric and material nonlinearity can be found in Appendix.

3.3 Parallel Computing- Efficient simulation using GPU

The numerical scheme outlined in the previous section is implemented through the use of Compute Unified Device Architecture (CUDA)[45], an Application Programming Interface(API) and a parallel computing platform, to leverage graphical processing units(GPU) capabilities. CUDA provides transparent access to the GPU hardware at a low level while minimising the programming complexity and the attainable efficiency was demonstrated with an FDTD case study performed by Pandala et.al [46], wherein a speed improvement of up to seventy times was reported in comparison with computer processing units(CPU). The authors also have earlier explored the capability to use CUDA based acceleration for linear wave propagation through the polycrystalline material for both two and three-dimensional models[47]. In the present scheme, in order to retain the information between successive timesteps, the two sets of displacement and velocity components are stored as global variables. The stress components are evaluated at individual grid points as local variables. The use of shared memory does not provide any acceleration as there is zero redundancy in memory transactions. All the computations have been carried out with NVIDIA Tesla K40C graphics card.
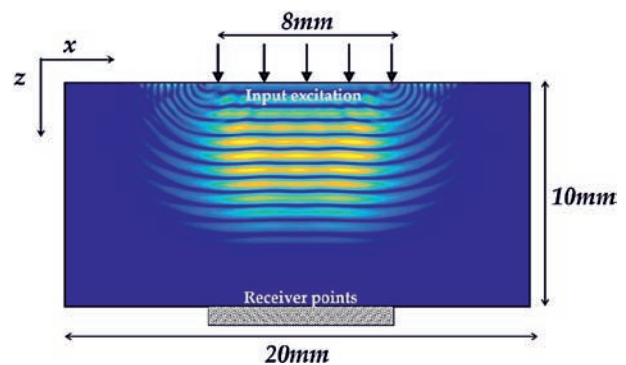

Fig. 3. Snapshot and Schematic diagram of a model for nonlinear elastic wave propagation.
Rys. 3. Schematyczne przedstawienie modelu do propagacji nieliniowej fali sprężystej

4. Numerical Modelling

4.1 Scheme

An FDTD simulation was carried out on a domain having dimension 20 mm x 10 mm. A Hann windowed tone burst signal of 5 MHz centre frequency with eight

cycles was imposed from the top surface of the domain. Hann windowed signal is known to produce significantly lower amplitudes (80dB) at the frequencies of harmonics of interest[21]. Through transmitted signal was received from the other end of the domain as shown in the schematic diagram in Figure 3. The length of the modelling domain was adjusted to isolate the first arrived signal from the side wall reflections at the receiver. The material properties used are for aluminium and are given in Table 2.[48].

Tab. 2. Material Properties used for Aluminum[48]
Tab. 2. Właściwości materiałowe aluminium [48]

Material	Aluminum
ρ	2727 kg/m³
λ	57.0 GPa
μ	27 GPa
A	-320 GPa
B	-200 GPa
C	-190 GPa

4.2 Gridding

It is known that RSG scheme requires at least 15 grid points per wavelength to avoid numerical dispersion and provide reasonable accuracy [40]. This criterion has been deduced from linear wave propagation considerations. It needs to be re-examined while dealing with nonlinear wave propagation involving generation of higher harmonic components. In the present study, we investigate the spatial sampling requirements to ensure sufficient modelling accuracy to extract up to third harmonics components from the numerical model. For the domain given in Figure 3, numerical simulation was performed for both GNL and MNL models by varying the grid point per wavelength as indicated in Figure 4. The peak amplitude of excitation here was set to 10^{-7}m. The received time domain signal was Fast Fourier transformed to extract the amplitudes of static, second and third harmonic components. Typical input and received time domain signal along with the corresponding frequency spectra are shown in Figure 5.

The grid convergence was obtained by calculating the difference between the amplitudes of individual harmonic component (i.e. static(A0), second(A2) and third(A3) harmonic component) to that of the converged solution Ac. The converged solution is obtained at the highest mesh density, in this case at $\lambda/50$. From, Figure 4 (a), for GNL model, it can be seen that both second harmonic and static displacement components converge beyond 30 grid points per wavelength. The presence of third harmonic components in this model was found to be minimal throughout and has hence been ignored from the present analysis and rest of the article. Figure 4 (b), which is for MNL, converges beyond 45 grids per wavelength. As static displacement component converges much earlier, ensuring the convergence for third harmonics will ensure sufficient sampling for static displacement components. General criteria for gridding and time stepping for GNL and MNL model is given in equation (24), (25) and (26)
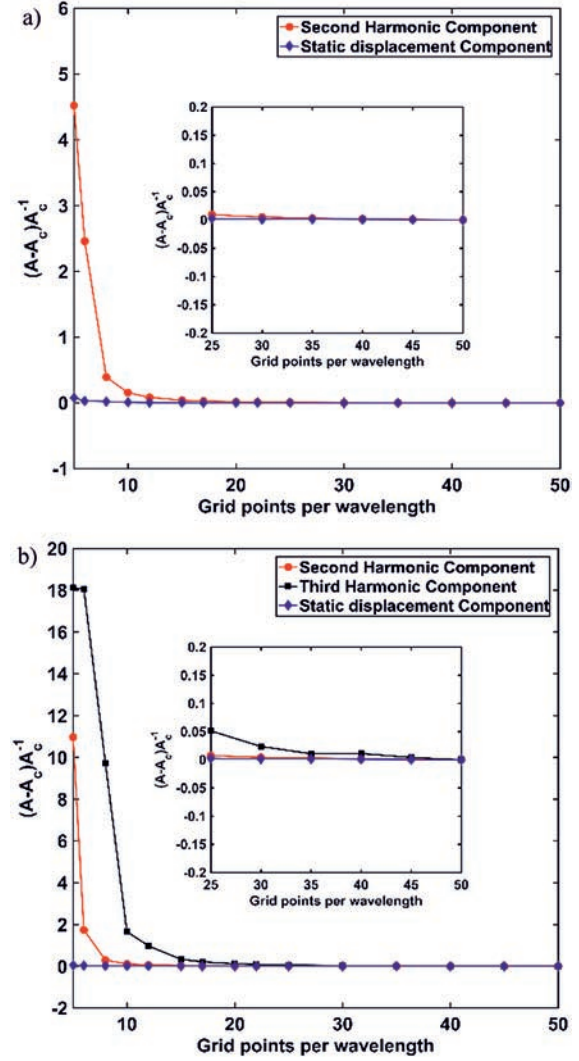

Fig. 4. Convergence of normalised harmonic amplitude against number of grid points per wavelength obtained for (a) GNL and (b) MNL models. A zoomed view of the graph near to the converging point is shown in the inset image. Results are presented for static displacement (blue diamond marker), second harmonic (red circular marker) and third harmonic component (black square marker).

Rys. 4. Zbieżność znormalizowanej amplitudy harmonicznej w funkcji liczby punktów siatki przypadających na długość fali, uzyskana dla modeli: (a) GNL, (b) MNL. W powiększeniu pokazano widok wykresu w pobliżu punktu zbieżności. Wyniki przedstawiono dla przemieszczenia statycznego (niebieski znacznik diamentowy), drugiej harmonicznej (czerwony znacznik kołowy) i trzeciej harmonicznej (czarny znacznik kwadratowy).

$$\lambda = \frac{V_{Lomgitudinal}}{f} \tag{24}$$

$$\Delta x = \Delta z = dh = \frac{1}{2} \times \left(\frac{\lambda}{15}\right)(GNL) \quad or \quad \frac{1}{3} \times \left(\frac{\lambda}{15}\right)(MNL) \tag{25}$$

$$\Delta t \leq \frac{\Delta h}{V_L \sum_{k=1}^{n}|c_k|} \tag{26}$$

where V_L is the longitudinal velocity in the material, λ is the longitudinal wavelength, Δh is the gridding, c_k represents difference coefficients(e.g. Holberg Coefficients[49]).
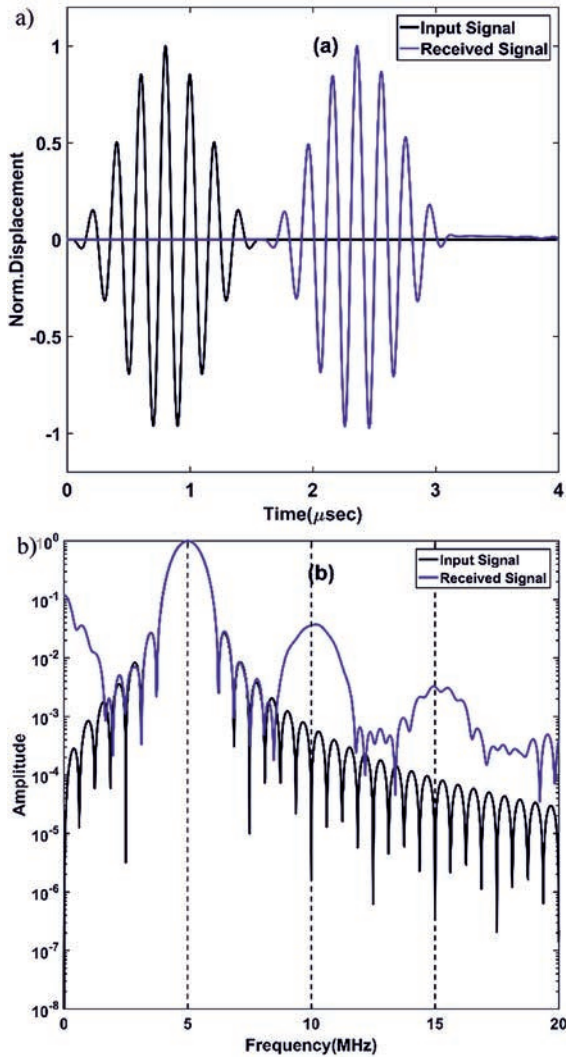
Fig. 5. (a) Typical input excitation and received A-scan signal (normalized) (a) corresponding FFT signal (normalized)
Rys. 5. Typowy znormalizowany sygnał wzbudzenia i wyjściowy: (a) w dziedzinie czasu (sygnał typu A) (b) w dziedzinie częstotliwości

4.3 Propagation Aspects

The solution to the nonlinear ultrasonic wave equation, based on an input harmonic wave train, has been deduced in numerous articles published earlier [15,19,21,50] and hence will not be repeated here. The expression for second harmonic nonlinear response (β) is given by

$$\beta = \frac{8v^2 A_2}{\omega^2 z A_1^2} \qquad A_2 \propto z A_1^2 \tag{27}$$

where β is the second-order nonlinear parameter, v is the longitudinal wave velocity of the material, ω is the angular frequency, z is the thickness of the material, A_1 is the fundamental amplitude, A_2 is the second harmonic amplitude.

Similarly, the third harmonic nonlinear parameter and the static displacement nonlinear parameter are given in Eq. (28) and (29)

$$\delta = \frac{24v^3 A_3}{\omega^3 z A_1^3} \qquad A_3 \propto z A_1^3 \tag{28}$$

$$\beta_{dc} = \frac{24v^2 A_{dc}}{\omega^2 z A_1^2} \qquad A_{dc} \propto z A_1^2 \tag{29}$$

where δ is the third order nonlinear parameter, β_{dc} is the static displacement nonlinear parameter, A_{dc} is the static displacement amplitude, A_3 is the third harmonic amplitude.
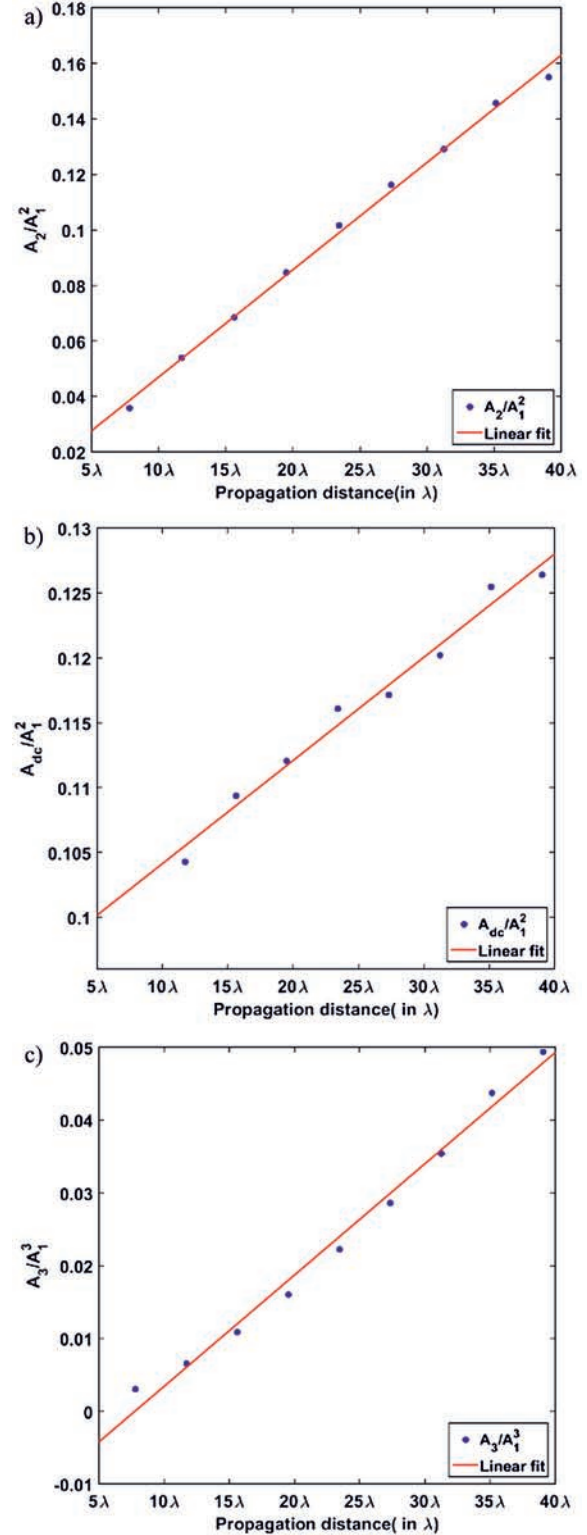

Fig. 6. Variation of (a) A_2/A_1^2, (b) A_{dc}/A_1^2 and (c) A_3/A_1^3 with propagation distance for MNL model
Rys. 6. Zależność (a) A_2/A_1^2, (b) A_{dc}/A_1^2, (c) A_3/A_1^3 od odległości dla modelu MNL
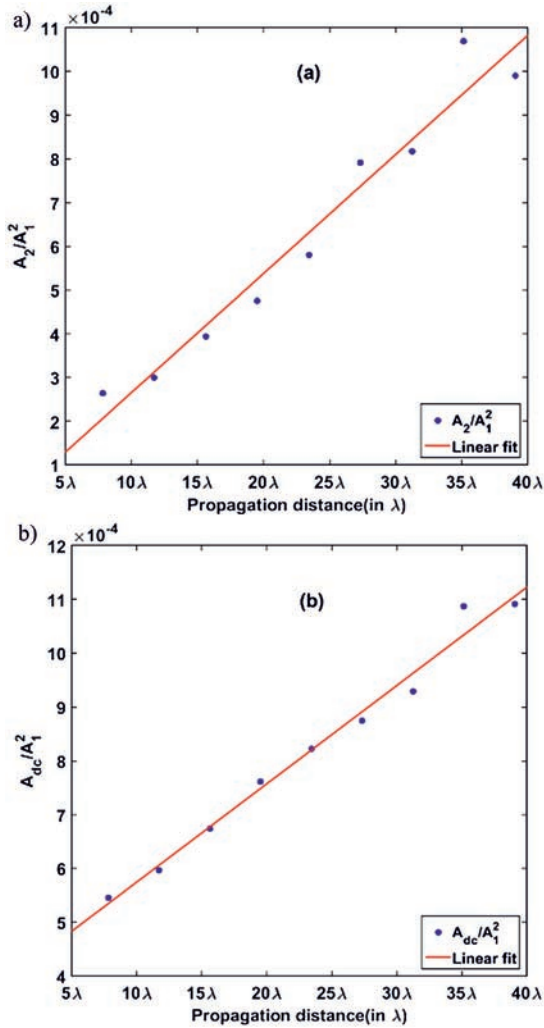
Fig. 7. Variation of (a) A_2/A_1^2 and (b) A_{dc}/A_1^2 with propagation distance for GNL model

Rys. 7. Zależność (a) A_2/A_1^2, (b) A_{dc}/A_1^2 od odległości dla modelu MNL

The stability and accuracy of the proposed FDTD model for nonlinear elastic media are demonstrated by performing simulation on medium with varying propagation distances using both the GNL and MNL models. It is expected from relations (27), (28) and (29) that the relative amplitude ratio, defined by A_2/A_1^2, A_{dc}/A_1^2 and A_3/A_1^3 would vary linearly over the propagation distances. The modelling parameters for this study have been kept similar to that mentioned in Section 4.1 while the propagation distance was varied from 10 mm to 50 mm. The frequency domain plots obtained for GNL and MNL models were individually normalised with respect to their corresponding amplitudes of the fundamental (A_1) and amplitudes corresponding to static, second and third harmonic components were extracted. This normalisation permits comparisons between the responses from different nonlinear models. The variation of A_2/A_1^2, A_{dc}/A_1^2 and A_3/A_1^3 with propagation distance for MNL model is shown in Figure 6. A similar plot for A_2/A_1^2 and A_{dc}/A_1^2 evaluated using the GNL model is shown in Figure 7. The linear trend indicates that the nonlinear effect captured by the numerical scheme is consistent with the theoretical expression for all three nonlinear parameters given in Eq. (27), (28) and (29)

As mentioned earlier, the contribution from third harmonics generated from GNL model was found to be negligibly small at the given input amplitude level and has been ignored from the analysis detailed in this section.

5. Results and discussions
5.1 Verification of FDTD model

We compare the MNL-FDTD model with an FE model implemented using a commercial software package, COMSOL Multiphysics 5.2 [51]. This commercial software package runs on an implicit solver and adopts a straightforward implementation of third-order elastic constants (TOEC's). In contrast, our FDTD model employs an explicit scheme, and the objective here is to draw a comparison in terms of the accuracy of the solution, as such packages have been widely utilised for the nonlinear wave propagation studies[20, 52, 53].The modelling parameters are kept identical for both the models and are shown in Table 2 and Table.3. The peak amplitude of input excitation was set of 10^{-7}m. Figure 8.(a) shows the time domain and FFT signal drawing a comparison between the FE and FDTD model. It can be seen that the time domain signals shows good agreement with each other showing a discrepancy within 1%. The FFT shown in Figure 8. (b) also indicates good agreement with the FE Model for static components, second harmonic and third harmonic components showing the differences to be less than 1% for the peak amplitudes. The simulation time for the FDTD model given in Table 3, was of the order of one minute, while the memory intensive model having a dimension 20 mm x 50 mm with 5MHz input frequency took 6 minutes.

Tab. 3. Simulation parameters used for comparing FE and FDTD models.

Tab. 3. Parametry symulacji używane do porównywania modeli FE i FDTD

	FE Model	F DTD Model
Model dimension	20 mm x 10 mm	
Input frequency/Number of cycles	5 MHz/ 8 cycles	
Step time/Gridding	3.4e-9sec / $\lambda_{longitudinal}$/45	

5.2 Comparison of Linear, GNL and MNL models

The amplitude of input displacement considered here is in the order of 10^{-7}m. Figure 9. (a) compares the time domain signal received for the three models. It can be seen that all the three models overlap with each other to a greater extent, while some fluctuations can be observed beyond the first arrived signal in case of MNL model (shown in the inset in Figure 9. (b)). This could indicate the presence of higher harmonic components as reported in Fig.7 of [20]. The frequency spectra shown in Figure 9. (c) indicate a higher harmonic contribution from MNL than GNL. Similar trends have been reported in the numerical model presented by Chillara and Lissenden [20].

The study was extended to investigate into the responses of the harmonic components by varying the input amplitude levels. Figure 10 shows frequency responses for MNL and GNL models, indicating consistent increment in the higher harmonic generation. At lower amplitude levels (in the order of 1e-9m), both GNL and MNL models, showed excellent

agreement with the linear elastic model, which indicates that noticeable harmonic components are generated only above certain finite amplitude levels. The static displacement component (or DC component) amplitudes are observed to be one order higher in MNL model in comparison with GNL model.
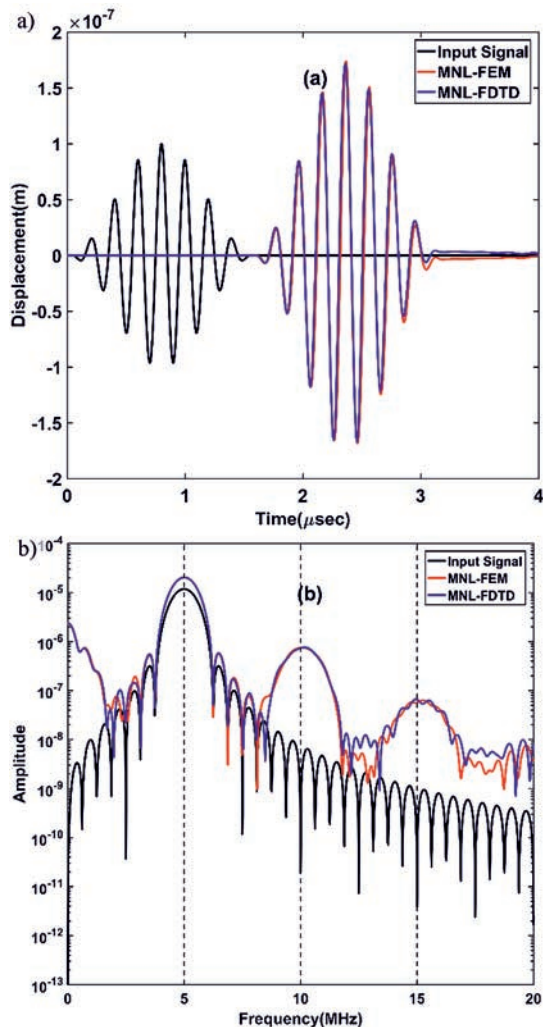

Fig. 8. Comparison of FEM and FDTD models with the input excitation signal (a) Time domain (b) FFT. Note the difference in the signal strength between input and output signal in the time domain are reflected in the FFT plot.

Rys. 8. Porównanie wyników modeli FEM i FDTD z wejściowym sygnałem wzbudzenia (a) w dziedzinie czasu (b) w dziedzinie częstotliwości. Uwaga: różnica w sile sygnału między sygnałem wejściowym i wyjściowym w dziedzinie czasu jest odzwierciedlona na wykresie widmowym.

6. Conclusions

The development of a robust numerical FDTD RSG scheme to deal with geometric and material nonlinearity in homogeneous isotropic materials has been described. The two bottlenecks of RSG scheme: large computational memory and extensive simulations times are addressed by adopting a Parsimonious scheme and parallelizing the time domain simulations on GPU with CUDA API. The simulation runtimes for the most memory-intensive test case of the FDTD model was of the order of six minutes.

The study also provides the required spatial sampling to ensure sufficient modelling accuracy to extract up to third harmonics as a guideline for future modelling. The time and frequency domain signals obtained from the proposed scheme are verified with the commercial available FE solver showing a discrepancy within 1%. The amplitude of the harmonic contents extracted has shown linear behaviour with propagation distance, underlying the stability and accuracy of the proposed modelling scheme. It is observed that the contribution of MNL model dominates the GNL model at a given input amplitude level and both GNL and MNL model behaves similar to the linear model at smaller input amplitude levels, which are in agreement with the existing numerical predictions[20].
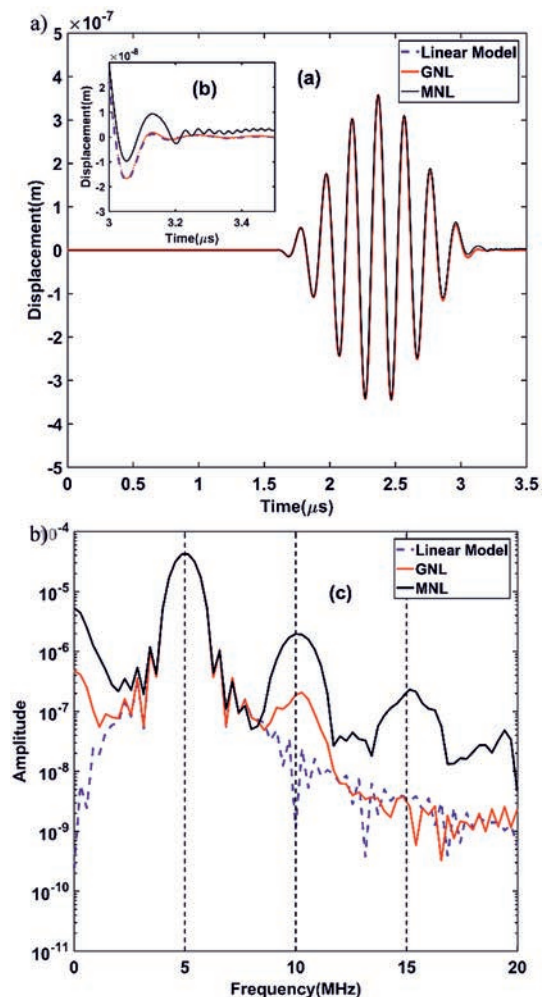

Fig. 9. Comparison of Response of Linear (blue dashed lines), GNL (red solid lines) and MNL (black solid lines) models for a peak to peak input excitation of the order 1e-7 m showing (a) Received time domain signal and (b) magnified view of the time domain signal shown in the inset shows the presence of extra frequency components (c) FFT of the received time domain signal for the corresponding models.

Rys. 9. Porównanie odpowiedzi modelu liniowego (niebieskie linie przerywane), GNL (czerwone linie ciągłe) i MNL (czarne linie ciągłe) dla wzbudzania wejściowego o wartości międzyszczytowej rzędu 10⁻⁷ m: (a) odebrany sygnał w dziedzinie czasu, (b) powiększony widok sygnału w dziedzinie czasu (obecność dodatkowych składowych częstotliwościowych), (c) wynik transformacji FFT odebranego sygnału dla badanych modeli.
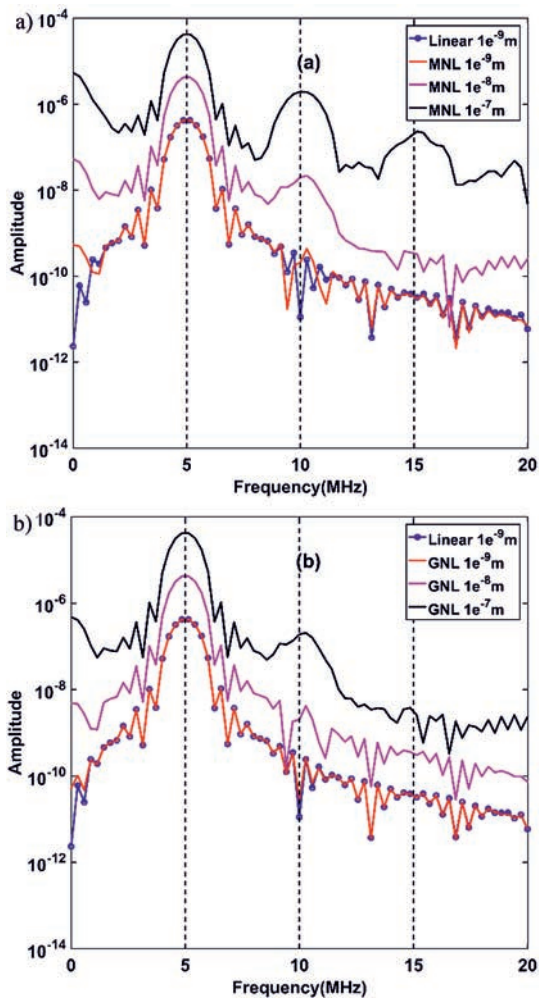
Fig. 10. Comparison of response of (a) Linear versus MNL (b) Linear versus GNL models for various orders of peak to peak input amplitudes. Results of the Linear models are shown in blue dashed lines with circular markers, and both MNL/GNL models are represented using solid lines.

Rys. 10. Porównanie odpowiedzi modeli dla różnych rzędów międzyszczytowej amplitudy sygnału wejściowego: (a) liniowy i MNL (b) liniowy i GNL. Wyniki modeli liniowych są przedstawione za pomocą niebieskich przerywanych linii z okrągłymi znacznikami, a oba modele MNL / GNL są reprezentowane za pomocą linii ciągłych.

As the RSG FDTD scheme is numerically stable with the existence of high contrast heterogeneities such as voids, cracks and inclusions, numerical investigation can be extended to understand the effect of microstructural inhomogeneities like micro-voids[54], micro-cracks, inclusions and precipitates[55] on acoustic nonlinearity parameter with appropriately measured second-order and third-order elastic constants[56].

Also, with the ability of RSG scheme to better handle anisotropic media, the current numerical scheme could also be adopted for studying the nonlinear wave propagation through polycrystalline media by incorporating the appropriate second and third-order elastic constants for each grain. The spatial sampling requirements derived earlier may not hold in this case, as grains are being often smaller compared to the probing wavelength, requiring much finer gridding than the aforementioned criteria.

7. References/Literatura

[1] M.A. Breazeale, D.O. Thompson, Finite-amplitude ultrasonic waves in aluminum, Appl. Phys. Lett. 3 (1963) 77–78. doi:10.1063/1.1753876.

[2] M.A. Breazeale, J. Ford, Ultrasonic studies of the nonlinear behavior of solids, J. Appl. Phys. 36 (1965) 3486–3490. doi:10.1063/1.1703023.

[3] P.A. Johnson, B. Zinszner, P.N.J. Rasolofosaon, Resonance and elastic nonlinear phenomena in rock, J. Geophys. Res. Solid Earth. 101 (1996) 11553–11564. doi:10.1029/96JB00647.

[4] L.A. Ostrovsky, P.A. Johnson, Dynamic nonlinear elasticity in geomaterials, Riv. Del. 24 (2001) 1–46. doi:10.1029/2002JB002038.

[5] I.Y. Solodov, N. Krohn, G. Busse, CAN: An example of nonclassical acoustic nonlinearity in solids, Ultrasonics. 40 (2002) 621–625. doi:10.1016/S0041-624X(02)00186-5.

[6] K.E.-A. Van Den Abeele, P.A. Johnson, A. Sutin, Nonlinear Elastic Wave Spectroscopy (NEWS) Techniques to Discern Material Damage, Part I: Nonlinear Wave Modulation Spectroscopy (NWMS), Res. Nondestruct. Eval. 12 (2000) 17–30. doi:10.1080/09349840009409646.

[7] G.D. Meegan, P.A. Johnson, R.A. Guyer, K.R. McCall, Observations of nonlinear elastic wave behavior in sandstone, J. Acoust. Soc. Am. 94 (1993) 3387–3391. doi:10.1121/1.407191.

[8] R.A. Guyer, K.R. McCall, K. Van Den Abeele, Slow elastic dynamics in a resonant bar of rock, Geophys. Res. Lett. 25 (1998) 1585–1588. doi:10.1029/98GL51231.

[9] E.H. Field, P.A. Johnson, I.A. Beresnev, Y. Zeng, Nonlinear ground-motion amplification by sediments during the 1994 Northridge earthquake, Nature. 390 (1997) 599–602. doi:10.1038/37586.

[10] R.A. Guyer, P.A. Johnson, The astonishing case of mesoscopic elastic nonlinearity, Phys. Today. 52 (1999) 30–35.

[11] R.T. Beyer, The Parameter B/A, in: D.. Hamilton, M. F. and Blackstrock (Ed.), Nonlinear Acoust., 1997: p. 25.

[12] B. Ward, A.C. Baker, V.F. Humphrey, Nonlinear propagation applied to the improvement of resolution in diagnostic medical ultrasound, J. Acoust. Soc. Am. 101 (1997) 143–154. doi:10.1121/1.417977.

[13] E.L. Carstensen, D.R. Bacon, Biomedical Applications, in: D.. Hamilton, M. F. and Blackstrock (Ed.), Nonlinear Acoust., 1997: p. 421.

[14] Y. Zheng, R.G. Maev, I.Y. Solodov, Nonlinear acoustic applications for material characterization: A review, Can. J. Phys. 77 (1999) 927–967. doi:10.1139/p99-059.

[15] A.N. Norris, Finite Amplitude waves in Solids, in: M. F. Hamilton and D. T. Blackstock (Ed.), Nonlinear Acoust., Academic press San Diego, 1998: pp. 263–277.

[16] V. Gusev, V. Tournat, B. Castagnède, Nonlinear Acoustic Phenomena in Micro-inhomogenous Media, in: Mater. Acoust. Handb., ISTE, 2009: pp. 431–471. doi:10.1002/9780470611609.ch17.

[17] O. V Rudenko, M.J. Crocker, Nonlinear Acoustics, in: Handb. Noise Vib. Control, John Wiley & Sons, Inc., 2007: pp. 159–168. doi:10.1002/9780470209707.ch10.

[18] Y. Zheng, R.G. Maev, I.Y. Solodov, Review / Syth?se Nonlinear acoustic applications for material characterization: A review, Can. J. Phys. 77 (2000) 927–967. doi:10.1139/p99-059.

[19] K.H. Matlack, J.Y. Kim, L.J. Jacobs, J. Qu, Review of Second Harmonic Generation Measurement Techniques for Material State Determination in Metals, J. Nondestruct. Eval. 34 (2015). doi:10.1007/s10921-014-0273-5.

[20] V.K. Chillara, C.J. Lissenden, Nonlinear guided waves in plates: A numerical perspective, Ultrasonics. 54 (2014) 1553–1558. doi:10.1016/j.ultras.2014.04.009.

[21] M.A. Drewry, P.D. Wilcox, One-dimensional time-domain finite-element modelling of nonlinear wave propagation for non-destructive evaluation, NDT E Int. 61 (2014) 45–52. doi:10.1016/j.ndteint.2013.09.006.

[22] N. Rauter, R. Lammering, Numerical simulation of elastic wave propagation in isotropic media considering material and geometrical nonlinearities, Smart Mater. Struct. 24 (2015) 45027. doi:10.1088/0964-1726/24/4/045027.

[23] Y.-X. Xiang, W.-J. Zhu, M.-X. Deng, F.-Z. Xuan, Experimental and numerical studies of nonlinear ultrasonic responses on plastic deformation in weld joints, Chinese Phys. B. 25 (2016) 24303. doi:10.1088/1674-1056/25/2/024303.

[24] F. Schubert, Numerical time-domain modeling of linear and nonlinear ultrasonic wave propagation using finite integration techniques--theory and applications., Ultrasonics. 42 (2004) 221–9. doi:10.1016/j.ultras.2004.01.013.

[25] N. Matsuda, S. Biwa, A Finite-Difference Time-Domain Technique for Nonlinear Elastic Media and Its Application to Nonlinear Lamb Wave Propagation, Jpn. J. Appl. Phys. 51 (2012) 07GB14. doi:10.1143/JJAP.51.07GB14.

[26] N. Matsuda, S. Biwa, Frequency dependence of second-harmonic generation in Lamb waves, J. Nondestruct. Eval. 33 (2014) 169–177. doi:10.1007/s10921-014-0227-y.

[27] J. Virieux, P-SV wave propagation in heterogeneous media:Veloctiy-stress finite difference method*, 51 (1986).

[28] J. Virieux, SH -wave propagation in heterogeneous media: Velocity-stress finite-difference method, GEOPHYSICS. 49 (1984) 1933–1942. doi:10.1190/1.1441605.

[29] E.H. Saenger, N. Gold, S. a. Shapiro, Modeling the propagation of elastic waves using a modified finite-difference grid, Wave Motion. 31 (2000) 77–92. doi:10.1016/S0165-2125(99)00023-2.

[30] H. Bao, J. Bielak, O. Ghattas, L.F. Kallivokas, D.R. O'Hallaron, J.R. Shewchuk, J. Xu, Large-scale simulation of elastic wave propagation in heterogeneous media on parallel computers, Comput. Methods Appl. Mech. Eng. 152 (1998) 85–102. doi:10.1016/S0045-7825(97)00183-7.

[31] D. Michéa, D. Komatitsch, Accelerating a three-dimensional finite-difference wave propagation code using GPU graphics cards, Geophys. J. Int. 182 (2010) 389–402. doi:10.1111/j.1365-246X.2010.04616.x.

[32] P. Huthwaite, Accelerated finite element elastodynamic simulations using the GPU, J. Comput. Phys. 257 (2014) 687–707. doi:10.1016/j.jcp.2013.10.017.

[33] P. Packo, T. Bielak, A.B. Spencer, T. Uhl, W.J. Staszewski, K. Worden, T. Barszcz, P. Russek, K. Wiatr, Numerical simulations of elastic wave propagation using graphical processing units—Comparative study of high-performance computing capabilities, Comput. Methods Appl. Mech. Eng. 290 (2015) 98–126. doi:10.1016/j.cma.2015.03.002.

[34] C. Truesdell, W. Noll, The Non-Linear Field Theories of Mechanics/Die Nicht-Linearen Feldtheorien der Mechanik, Springer Science & Business Media, 2013.

[35] J.L. Rose, Ultrasonic waves in solid media, Cambridge university press, 2004.

[36] R.S. Mini, Wave Propagation Through Microstructural Features with Geometric Nonlinearity- Experimental and Numerical Investigations, Indian Institute of Technology Madras, 2016.

[37] L.D. Landau, E.M. Lifshitz, A.M. Kosevich, L.P. Pitaevskiæi, Theory of Elasticity, 3rd, (1986).

[38] E.H. Saenger, T. Bohlen, Finite-difference modeling of viscoelastic and anisotropic wave propagation using the rotated staggered grid, Geophysics. 69 (2004) 583–591. doi:10.1190/1.1707078.

[39] H. Igel, P. Mora, B. Riollet, Anisotropic wave propagation through finite difference grids, GEOPHYSICS. 60 (1995) 1203–1216. doi:10.1190/1.1443849.

[40] V. Lisitsa, D. Vishnevskiy, Lebedev scheme for the numerical simulation of wave propagation in 3D anisotropic elasticity‡, Geophys. Prospect. 58 (2010) 619–635. doi:10.1111/j.1365-2478.2009.00862.x.

[41] P. Moczo, J. Kristek, E. Bystrický, Efficiency and optimization of the 3-D finite-difference modeling of seismic ground motion, J. Comput. Acoust. 9 (2001) 593–609.

[42] Y. Luo, G. Schuster, Parsimonuis staggered grid Finite-Differencing of the wave equation, Geophys. Res. Lett. 17 (1990) 155–158.

[43] J. Zhang, T. Liu, Elastic wave modelling in 3D heterogeneous media: 3D grid method, Geophys. J. Int. 150 (2002) 780–799. doi:10.1046/j.1365-246X.2002.01743.x.

[44] K.R. Kelly, R.W. Ward, S. Treitel, R.M. Alford, Synthetic Seismograms: A Finite Difference Approach, Geophysics. 41 (1976) 2–27. doi:10.1190/1.1440605.

[45] NVIDIA, CUDA C Programming guide, (n.d.). http://docs.nvidia.com/cuda/cuda-c-programming-guide/index.html.

[46] A. Pandala, K. Balasubramaniam, M. Spies, Simulation of Ultrasonic Inspection of Complex Components Using a 3D-FDTD-Approach, in: Proc. 19th WCNDT, 2016: pp. 3–10.

[47] A. Pandala, S. Shivaprasad, C. V Krishnamurthy, K. Balasubramaniam, Modelling of Elastic Wave Scattering in Polycrystalline Materials, in: 8th Int. Symp. NDT Aerosp., 2016.

[48] W.J.N. De Lima, M.F. Hamilton, Finite-amplitude waves in isotropic elastic plates, J. Sound Vib. 265 (2003) 819–839. doi:10.1016/S0022-460X(02)01260-9.

[49] O. Holberg, Computational Aspects Of The Choice Of Operator And Sampling Interval For Numerical Differentiation In Large-Scale Simulation Of Wave Phenomena, Geophys. Prospect. 35 (1987) 629–655. doi:10.1111/j.1365-2478.1987.tb00841.x.

[50] A. Hikata, B.B. Chick, C. Elbaum, Dislocation contribution to the second harmonic generation of ultrasonic waves, J. Appl. Phys. 36 (1965) 229–236. doi:10.1063/1.1713881.

[51] COMSOL, Introduction To COMSOL Multiphysics, (2016). cdn.comsol.com/documentation/5.2.0.166/IntroductionToCOMSOLMultiphysics.pdf.

[52] S. Delrue, K. Van Den Abeele, Three-dimensional finite element simulation of closed delaminations in composite materials, Ultrasonics. 52 (2012) 315–324. doi:10.1016/j.ultras.2011.09.001.

[53] J. Zhao, V.K. Chillara, B. Ren, H. Cho, J. Qiu, C.J. Lissenden, Second harmonic generation in composites: Theoretical and numerical analyses, J. Appl. Phys. 119 (2016) 64902. doi:10.1063/1.4941390.

[54] J.S. Valluri, K. Balasubramaniam, R. V. Prakash, Creep damage characterization using non-linear ultrasonic techniques, Acta Mater. 58 (2010) 2079–2090. doi:10.1016/j.actamat.2009.11.050.

[55] Y. Xiang, M. Deng, F.Z. Xuan, C.J. Liu, Effect of precipitate-dislocation interactions on generation of nonlinear Lamb waves in creep-damaged metallic alloys, J. Appl. Phys. 111 (2012). doi:10.1063/1.4720071.

[56] R.N. Thurston, K. Brugger, Third-Order Elastic Constants and the Velocity of Small Amplitude Elastic Waves in Homogeneously Stressed Media, Phys. Rev. 135 (1964) AB3-AB3. doi:10.1103/PhysRev.135.AB3.2.

8. Appendix

The following discretized equations are valid for interior of the solid. At the boundaries, the computation of velocity is performed by replacing the central finite differences with either forward (or backward) finite differences. The partial derivatives and represented by $\frac{\partial}{\partial x}$ and $\frac{\partial}{\partial z}$ are computed as follows

$$D_x P_{ik}^l = \frac{P_{i+1/2,k+1/2}^l - P_{i-1/2,k-1/2}^l + P_{i-1/2,k+1/2}^l - P_{i+1/2,k-1/2}^l}{2\Delta x} \tag{30}$$

$$D_z P_{ik}^l = \frac{P_{i+1/2,k+1/2}^l - P_{i-1/2,k-1/2}^l - P_{i-1/2,k+1/2}^l + P_{i+1/2,k-1/2}^l}{2\Delta z} \tag{31}$$

where *P* is the variable of interest, subscript $i = x,z$; $k = x,z$ and superscipt represents timesteps.

Geometric Nonlinearity

The complete set of discretized equations (7-9), (20-23) for geometric nonlinear model described in Section 2.2 are given by

$$\tau^l_{xx|i,k} = \frac{\lambda+2\mu}{2}\left[2D_x u^l_{x|i,k} - \left(D_x u^l_{x\,i,k}\right)^2 - \left(D_x u^l_{z|i,k}\right)^2\right] + \frac{\lambda}{2}\left[2D_z u^l_{z|i,k} - \left(D_z u^l_{x|i,k}\right)^2 - \left(D_z u^l_{z|i,k}\right)^2\right] \quad (32)$$

$$\tau^l_{xz|i,k} = \tau^l_{zx,k} = \mu\left[D_z u^l_{x|i,k} + D_x u^l_{z|i,k} - D_x u^l_{x|i,k}D_z u^l_{x\,i,k} - D_x u^l_{z|i,k}D_z u^l_{z|i,k}\right] \quad (33)$$

$$\tau^l_{xz|i,k} = \tau^l_{zx\,i,k} = \mu\left[D_z u^l_{x|i,k} + D_x u^l_{z|i,k} - D_x u^l_{x|i,k}D_z u^l_{x\,i,k} - D_x u^l_{z|i,k}D_z u^l_{z\,i,k}\right] \quad (34)$$

$$v^{l+1/2}_{x|i,k} = v^{l-1/2}_{x|i,k} + (1/\rho)\left(D_x \tau^l_{xx|i,k} + D_x \tau^l_{xz|i,k}\right)$$

$$v^{l+1/2}_{z|i,k} = v^{l-1/2}_{z|i,k} + (1/\rho)\left(D_z \tau^l_{xz|i,k} + D_z \tau^l_{zz|i,k}\right) \quad (35)$$

$$u^{l+1}_{x|i,k} = u^l_{x|i,k} + dt\left(v^{l+1/2}_{x|i,k}\right) \quad (36)$$

$$u^{l+1}_{y|i,k} = u^l_{y|i,k} + dt\left(v^{l+1/2}_{y|i,k}\right) \quad (37)$$

Material Nonlinearity

The constitutive equations (15-18), elastodynamic equations (20-23) for material nonlinear model when discretized take the following form

$$\tau^l_{xx\,i,k} = c_{11}D_x u^l_{x|i,k} + c_{12}D_z u^l_{z|i,k} + d_1\left(D_x u^l_{x|i,k}\right)^2 + d_2\left(2D_x u^l_{x\,i,k} + D_z u^l_{z|i,k}\right)D_z u^l_{z\,i,k} + d_3\left(\left(D_z u^l_{x\,i,k}\right)^2 + \left(D_x u^l_{z|i,k}\right)^2\right) + d_3\left(D_z u^l_{x\,i,k}D_x u^l_{z|i,k}\right) \quad (38)$$

$$\tau^l_{zz|i,k} = c_{11}D_z u^l_{z|i,k} + c_{12}D_x u^l_{x|i,k} + d_1\left(D_z u^l_{z\,i,k}\right)^2 + d_2\left(2D_z u^l_{z\,i,k} + D_x u^l_{x|i,k}\right)D_x u^l_{x\,i,k} + d_3\left(\left(D_x u^l_{z|i,k}\right)^2 + \left(D_z u^l_{x|i,k}\right)^2\right) + d_3\left(D_z u^l_{x\,i,k}D_x u^l_{z|i,k}\right) \quad (39)$$

$$\tau^l_{xz\,i,k} = c_{44}\left(D_z u^l_{x|i,k} + D_x u^l_{z\,i,k}\right) + \left(D_x u^l_{x\,i,k} + D_z u^l_{z\,i,k}\right)\left(2d_3 D_z u^l_{x|i,k} + d_4 D_x u^l_{z\,i,k}\right) \quad (40)$$

$$\tau^l_{zx\,i,k} = c_{44}\left(D_z u^l_{x|i,k} + D_x u^l_{z\,i,k}\right) + \left(D_x u^l_{x\,i,k} + D_z u^l_{z|i,k}\right)\left(2d_3 D_x u^l_{z|i,k} + d_4 D_z u^l_{x\,i,k}\right) \quad (41)$$

$$v^{l+1/2}_{x\,i,k} = v^{l-1/2}_{x|i,k} + (1/\rho)\left(D_x \tau^l_{xx|i,k} + D_x \tau^l_{xz|i,k}\right) \quad (42)$$

$$v^{l+1/2}_{z|i,k} = v^{l-1/2}_{z|i,k} + (1/\rho)\left(D_z \tau^l_{zx|i,k} + D_z \tau^l_{zz|i,k}\right) \quad (43)$$

$$u^{l+1}_{x|i,k} = u^l_{x|i,k} + dt\left(v^{l+1/2}_{x|i,k}\right) \quad (44)$$

$$u^{l+1}_{y|i,k} = u^l_{x|i,k} + dt\left(v^{l+1/2}_{y\,i,k}\right) \quad (45)$$